Computational Materials Science 202 (2022) 110959

Contents lists available at ScienceDirect

Computational Materials Science

journal homepage: www.elsevier.com/locate/commatsci

Ab initio calculation of electron temperature dependent electron heat capacity and electron-phonon coupling factor of noble metals

Yongnan Li, Pengfei Ji *

Jinggong College, Beijing Institute of Technology, Beijing 100081, People's Republic of China

ARTICLE INFO

Keywords:
Electron heat capacity
Electron-phonon coupling factor
Ab initio calculation
Density-functional theory
Noble metals

ABSTRACT

Noble metal nanoparticles show fantastic catalytic property in various practical applications. It is a promising way to obtain nanoparticles from femtosecond laser ablation of noble metals. The calculation concentrates on electron heat capacity and electron–phonon coupling factor, which are two pivotal parameters describing the femtosecond laser-induced electron heating and the electron–phonon coupled energy transportation. The evolutions of these two parameters with increasing electron temperature are presented. It is found that the evolutions of the electron heat capacity and electron–phonon coupling factor are mainly affected by the electron density of states and the Fermi-Dirac distribution function.

1. Introduction

Since the reliable femtosecond lasers became available up to the year 2000 [1], owing to high average power and ultrashort pulse duration, the implementations of femtosecond laser are put into practical material processing and investigations on material properties [2–6]. When femtosecond laser irradiates on the surface of a given material, the first response of the target metal is the nonequilibrium excited electron. The diffusion of the temporally deposited laser energy in the electron subsystem is induced by electron–electron collisions, which takes a few tens of femtoseconds [5–8]. Due to the timescale of electron–phonon interaction is in picosecond [8,9], the electron temperature T_e elevates to tens of thousands of temperatures in Kelvin. However, the lattice subsystem retains in a relative cold state in femtosecond timescale [7,8,10,11]. Accompanying with the transportation of absorbed laser energy from the electron subsystem to lattice subsystem, the decrease of T_e and the increase of lattice temperature T_l happens [6,7]. Eventually, electrons and lattice equilibrate to same temperature as a result of the electron–phonon coupling, which brings out the phase change and laser ablation [6,7].

Theoretical descriptions and calculations of the femtosecond laser material interaction are essential to control the whole fabrication procedure. When it comes to the multiscale simulation, the two-temperature model (TTM) combined with molecular dynamics (MD) is employed [12,13]. The TTM model is widely applied to describe the temporal evolution of the deposited laser energy in the electron subsystem and its transportation to the lattice subsystem. Meanwhile, MD is utilized to describe the atomistic motion. There are several important parameters, such as the electron heat capacity C_e and electron–phonon coupling factor G_{e-ph}, which significantly influence T_e and T_l induced by laser energy deposition and electron–phonon coupled energy transportation.

The T_e dependences of $C_e = \int \left(g \frac{\partial f}{\partial T_e} + f \frac{\partial g}{\partial T_e} \right) \varepsilon d\varepsilon$ [14] and $G_{e-ph} = \frac{\pi \hbar k_B \lambda \langle \omega^2 \rangle}{g(\varepsilon_F)} \int g^2(\varepsilon) \left(-\frac{\partial f}{\partial \varepsilon} \right) d\varepsilon$ [8,15] have drawn increasing attentions. It is worth to draw attention to $\partial f / \partial T_e$ in the expression of C_e and $-\partial f / \partial \varepsilon$ in the expression of G_{e-ph}. $f = \left[1 + \exp\left(\frac{\varepsilon - \mu}{k_B T_e} \right) \right]^{-1}$ refers to the Fermi-Dirac distribution function. The alteration of electron distribution is due to f. Therefore, the variation of f influences C_e and G_{e-ph} with the increase of T_e. Furthermore, the impact of electron density of states g should be taken into account within the above expressions of both C_e and G_{e-ph}. To simplify the calculation of C_e and G_{e-ph} at low T_e, a linear T_e dependent approximation of C_e was given by Ashcroft *et al.* [16], and a constant calculation of G_{e-ph} was given by Wang *et al.* [17] based on the expression from Allen [18]. However, in order to obtain precise calculations of C_e and G_{e-ph}, a great number of research shown the comparison between linear-/nonlinear-dependence for various kinds of materials [19–26]. According to their results, there is a massive gap at high T_e between the linear dependent cases and the experimental

* Corresponding author.
E-mail address: PengfeiJi2HTEC@outlook.com (P. Ji).

https://doi.org/10.1016/j.commatsci.2021.110959
Received 12 July 2021; Received in revised form 1 October 2021; Accepted 5 October 2021
Available online 19 October 2021

results. Hence, the accurate calculations of T_e dependent C_e and G_{e-ph} are of great importance and significance for the femtosecond laser material interaction.

The dependences of C_e and G_{e-ph} at electron excitation were extensively investigated, such as gold (Au) [6–9,15,27–30], silver (Ag) [15,27,28,31,32] and platinum (Pt) [7,9,15,33,34]. There are a considerable amount of work studying the optical properties (reflective index, phonon dispersion, etc.) and electrical conductivity for Au [8,35–37], Ag [35–38] and Pt [39–41]. However, others noble metals, such as palladium (Pd), iridium (Ir), and rhodium (Rh), which are elements in the platinum-group were rarely studied. These noble metals show analogous chemical properties, generally used as catalysts in a lot of industrial applications [42]. Nano-size Pd is used to ameliorate hydrogen storage capacity [43]. Furthermore, Pd-based materials have great catalytic activity for producing hydrogen polymer electrolyte fuel cells [44]. Ir is getting attention with its great conductivity, stability and anticorrosion ability [45], which can be employed in sustainable electric power technologies, particularly for the production of polymer electrolyte membrane fuel cells [46]. Pd and Rh can be applied as active components of autocatalytic converters to restrict the emission of pollutants to the environment [47]. A bunch of research reported that the size and shapes of a nanoparticle can be controlled by the operational laser fabrication process [48–50]. Moreover, the size of nanoparticles produced by femtosecond laser ablation is much concentrated and smaller than that produced by nanosecond laser ablation [50]. Besides, the smaller size of catalysts is appropriate to improve catalytic performance by increasing contact area [51]. Therefore, it is practicable to synthesize nanoparticles of noble metals by femtosecond laser in order to enhance catalytic performance. In addition, a similar approach to fabricate Pd nanoparticles in liquid is presented by Nishi *et al.* [43], which shown the validity of femtosecond laser processing for noble metals. For the demand of producing noble metal nanoparticle by femtosecond laser irradiation, the precise calculations of electron thermophysical properties of Pd, Ir, and Rh in excited electron state are desired and indispensable.

In this study, a systematic computation and analysis of C_e and G_{e-ph} of Au, Pd, Ir, and Rh is presented by applying the *ab initio* method based on density-functional-theory (DFT). It is worth noting that the present work focuses on the electron heat capacity and the electron–phonon coupling factor in the states of hot electron subsystem and cold lattice subsystem, which occurs in tens of femtoseconds. Section 2 presents the derivations and description of the theoretical model. Section 3 gives the results and discussions of the calculated results. Before the calculations of C_e and G_{e-ph}, the theoretical calculations of g for the four noble metals are performed firstly. Eventually, a brief conclusion is presented in Section 4 to show the applicability of the model and the significance of the obtained results.

2. Theoretical model

2.1. Electron density of states

As the initial part of modeling, the quantification of g is indispensable. By solving the Schrödinger equation with DFT, g for the noble metals (Au, Pd, Ir, and Rh) were calculated firstly. The results of g are essential to carry out the subsequent calculations of C_e and G_{e-ph}. The calculation of g in the present work was performed with the DFT code ABINIT [22]. In the *ab initio* calculation, norm-conserving pseudopotentials using the Perdew–Burke–Ernzerhof (PBE) generalized-gradient approximation and PBE exchange–correlation functional were applied. Tests for the selection of PBE and local density approximation (LDA) are presented in Supplementary Material. As for the detailed description of the calculation, the lattice constants, cutoff energy, and number of DFT bands are shown in Table 1. The calculated lattice constants were compared with the results in [52], as shown in Table S1 in Supplementary Material. To increase the accuracy and efficiency of the calculations, the Monkhorst-Pack **k**-point sampling mesh of 16 × 16 × 16 was used to describe the Brillouin zone to obtain highly converged results. The convergence tests of the above parameters are seen in Supplementary Material.

Table 1
Parameters in the *ab initio* calculation.

	Au	Pd	Ir	Rh
Electron Structure	$6s^1 5d^{10}$	$4d^{10}$	$6s^2 5d^7$	$5s^1 4d^8$
a_0(Å)	4.050	3.842	3.814	3.758
DFT bands	32	32	32	32
Cutoff Energy(Ha)	52	52	60	46

2.2. Electron heat capacity

According to the definition of C_e, it refers to the rate of change of internal energy in the electron subsystem with T_e in a unit volume [16]. In order to obtain an accurate description of C_e, the influences of both T_e dependent f and g were taken into account, namely [14]

$$C_e|_{T_e} = \int_{-\infty}^{+\infty} \left(g|_{T_e} \frac{\partial f|_{T_e}}{\partial T_e} + f|_{T_e} \frac{\partial g|_{T_e}}{\partial T_e} \right) \varepsilon d\varepsilon \tag{1}$$

where $g|_{T_e}$ and $f|_{T_e}$ denote the electron density of states and the Fermi-Dirac distribution function at ε at T_e, respectively. At low T_e, a linear approximation of C_e is conventionally used, given by the free electron gas model [16]. The expression of the linear factor $\gamma = \pi^2 k_B^2 g(\varepsilon_F)/3$ shows that the factor is affected by g at Fermi energy ε_F. It makes a well description for noble metals at low T_e [16]. Considering the impact of f at low T_e, the value of f becomes to 0 in the energy state ε larger than ε_F. In other words, f can be regarded as step function, it means that few electrons occupy energy states above ε_F. But this approximation is invalid at high T_e, an unneglectable number of electrons occupy energy states above the threshold of ε_F. Thus, the invalidity of the simplified treatment of $C_e = \gamma T_e$ becomes a challenge. Thereby, a full representation of the C_e in Eq. (1) becomes a must. Alternatively, Equation (1) can also be expressed as

$$C_e|_{T_e} = \left(\frac{\partial E_{int}|_{T_e}}{\partial T_e} \right)_V \tag{2}$$

where E_{int} is the internal energy of the electron subsystem in a unit volume.

2.3. Electron-phonon coupling factor

The rate of energy transporting from the electron subsystem to the lattice subsystem per unit cell volume is proportional to the difference between T_e and T_l induced by the electron–phonon collisions [8,15,17,18]

$$\left. \frac{\partial E_e}{\partial t} \right|_{T_e} = G_{e-ph}|_{T_e} (T_e - T_l) \tag{3}$$

According to Allen [18], given the change of the electron and phonon distributions with the electron–phonon collision, the rate of energy transportation can be defined

$$\left. \frac{\partial E_e}{\partial t} \right|_{T_e} = \frac{4\pi}{\hbar} \sum_{kk'} \hbar\omega_Q \left[|M_{kk'}||_{T_e} \right]^2 [S(k,k')] \delta(\varepsilon_k - \varepsilon_{k'} + \hbar\omega_Q) \tag{4}$$

where k and Q refer to the quantum numbers of electrons and phonons, respectively. ε_k and $\varepsilon_{k'}$ are the energy of an electron in state k and k'. $\hbar\omega_Q$ is the phonon energy with frequency ω_Q. $M_{kk'}$ refers to the electron–phonon scattering matrix element, which indicates the scattering

probability. $S(k,k^{'})$ is the thermal factor exhibiting the emission and absorption process of phonon during the electron–phonon collision, which is defined from the electron and phonon occupation numbers with f and the Bose distribution function $n = \left[\exp(\frac{\hbar\Omega}{k_B T_l}) + 1\right]^{-1}$. Namely, $S(k, k^{'})$ equals to $(f_k - f_{k^{'}})n_Q - f_{k^{'}}(1 - f_k)$.

Following the suggestions by Allen [18] and Wang *et al.* [17], the Eliashberg spectral function $\alpha^2F(\varepsilon,\varepsilon^{'},\Omega)$ was used to simplify Eq. (4)

$$\left.\frac{\partial E_e}{\partial t}\right|_{T_e} = 2\pi g(\varepsilon_F)|_{T_e}\int_0^{\infty} d\Omega\hbar\Omega\int d\varepsilon\int d\varepsilon^{'}\alpha^2F(\varepsilon,\varepsilon^{'},\Omega)\left[n(\Omega)|_{T_l} - n(\Omega)|_{T_e}\right] \tag{5}$$

where $g(\varepsilon_F)|_{T_e}$ and $n(\Omega)|_{T_e}$ are the electron density of states at Fermi energy ε_F and the Bose distribution function at Ω, respectively. By applying the approximation $\alpha^2F(\varepsilon,\varepsilon^{'},\Omega) = \frac{g(\varepsilon)g(\varepsilon^{'})}{g(\varepsilon_F)^2}\alpha^2F(\Omega)$ [15,17] and simplifying with the thermal factor as $(f_k - f_{k^{'}})\left[n(\varepsilon_{k^{'}} - \varepsilon_k)|_{T_l} - n(\varepsilon_k - \varepsilon_{k^{'}})|_{T_e}\right]$ [8], Eq. (5) becomes

$$\left.\frac{\partial E_e}{\partial t}\right|_{T_e} = 2\pi g(\varepsilon_F)|_{T_e}\int_0^{\infty} d\Omega(\hbar\Omega)^2\alpha^2F(\Omega)\int d\varepsilon\int d\varepsilon^{'}\frac{g(\varepsilon)|_{T_e}g(\varepsilon^{'})|_{T_e}}{\left[g(\varepsilon_F)|_{T_e}\right]^2}S(\varepsilon,\varepsilon^{'}) \tag{6}$$

where $g(\varepsilon_F)|_{T_e}$, $g(\varepsilon)|_{T_e}$ and $g(\varepsilon^{'})|_{T_e}$ are the electron density of states in energy states of ε_F, ε and $\varepsilon^{'}$, respectively. Furthermore, the second moment of the Eliashberg spectral function $\lambda\langle\omega^2\rangle = 2\int_0^{\infty} d\Omega\alpha^2F(\Omega)\Omega$ is used to simplified Eq. (6), then an integral expression of the rate of energy transferring from the electron subsystem to the lattice subsystem is derived [15]. Thereby, T_e dependent G_{e-ph} in Eq. (3) becomes

$$G_{e-ph}|_{T_e} = \frac{\pi\hbar k_B\lambda\langle\omega^2\rangle}{g(\varepsilon_F)|_{T_e}}\int\left[g(\varepsilon)|_{T_e}\right]^2\left(-\frac{\partial f|_{T_e}}{\partial\varepsilon}\right)d\varepsilon \tag{7}$$

Compared with the constant expression of $G_{e-ph} = G_0 = \pi\hbar k_B g(\varepsilon_F)|_{300\ \mathrm{K}}\lambda\langle\omega^2\rangle$ given by Wang *et al.* at $T_e = 300$ K [15,17], the integral $\int\left[g(\varepsilon)|_{T_e}\right]^2\left(-\frac{\partial f|_{T_e}}{\partial\varepsilon}\right)d\varepsilon$ from Eq. (7) can be approximated as $\int\left[g(\varepsilon)|_{T_e}\right]^2\delta(\varepsilon-\varepsilon_F)d\varepsilon = \left[g(\varepsilon_F)|_{T_e}\right]^2$, subsequently obtains the same expression. However, the deviation of aforementioned approximations applied for Eq. (7) was pointed out in [7,8,15,17], which mainly concentrates on the determination of the $\alpha^2F(\Omega)$. The simplification $\alpha^2F(\varepsilon,\varepsilon^{'},\Omega) = \frac{g(\varepsilon)g(\varepsilon^{'})}{g(\varepsilon_F)^2}\alpha^2F(\Omega)$ is based on an assumption of constant $M_{kk^{'}}$ in electron states k and $k^{'}$. It is generally derived by the calculation of the excited electron decay rate induced by phonon [15]. In the present work, the density-functional perturbation theory (DFPT) was applied to get $\alpha^2F(\Omega)$. The calculation was carried out through the responses of the system with atomic displacements and homogeneous electric fields [22,53]. Considering the electron states dependence of $M_{kk^{'}}$, the value of $M_{kk^{'}}$ was determined by interpolation in the present work [22]. Combining with g and f mentioned in the first part in this section, G_{e-ph} was calculated accurately from Eq. (7). An $8\times8\times8$ **q**-point mesh was used for the phonon calculation. After the phonon calculation, the calculations of $M_{kk^{'}}$ are implemented with **q**-point mesh of $8\times8\times8$ by interpolation.

3. Results and discussion

3.1. Electron density of states and the Fermi-Dirac distribution at different electron temperature

The calculation results of g at T_e of 300 K, 5,000 K, 10,000 K and 20,000 K are shown in Fig. 1(a)-(d). The zero point of the energy scale

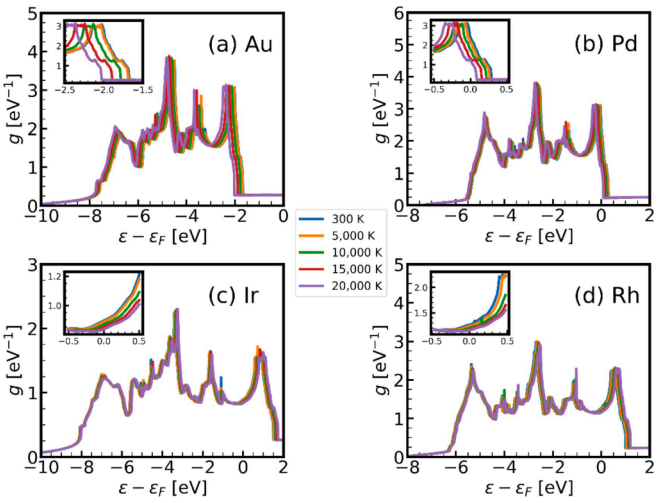

Fig. 1. Electron density of states g for (a) Au, (b) Pd, (c) Ir, and (d) Rh for electron temperature T_e at 300 K, 5,000 K, 10,000 K and 20,000 K.

was set as ε_F, which was obtained from the chemical potential μ at 0 K. The common characteristic of the electron structure of given metals is the presence of d block, as shown in Table 1.

For the case of Au with 5d block fully occupied by electrons, the increase of T_e induces an electron transfer from 5d block to 6s block, then causes a decrease of electronic screening and a more attractive electron–ion potential, eventually it causes a shrinkage of 5d block and a global shift of g toward lower energies [9,25], as displayed in Fig. 1(a). At low T_e, the 6s electrons are excited merely, thus the first peak to the left of the zero point is close to the zero point. By contrast, as more electrons (particularly 5d electrons) are excited at high T_e, the left shift of g is observed. Namely, the smearing of f appears. As the impact induced by smearing of f and left shift of g, μ magnifies with the increase of T_e to preserve constant number of valence electrons [8,9,14], as shown in the inset of Fig. 2(a). Therefore, the T_e dependent variation of f is reflected in aspects of T_e and T_e dependent μ in the expression $f = \left[1 + \exp(\frac{\varepsilon-\mu}{k_B T_e})\right]^{-1}$, as shown in Fig. 2(a).

Considering the cases of Pd, significant difference of g from the case of Au is observed. In Fig. 1(b), despite filled d block of Pd analogous to that of Au, the high-energy edge of g locates at the right side of zero point at low T_e and a high density of states at zero point is observed. However, similar to Au, the shift of g toward lower energy state with increasing T_e is observed, which is attributed to the vast thermal excited 4d electrons. Eventually, the high-energy edge of g shifts to the left of zero point. In addition, the inset of Fig. 2(b) shows growth tendency of μ for Pd. The variation of μ for Pd is consistent with the left shifts of g with increasing T_e, as same as the case of Au.

Due to the partially filled 5d and 4d block of Ir and Rh, huge differences from the case of Au are observed. As seen in Fig. 1(c) and 1(d), the high-energy edges of g for both two metals locate at the right of zero point, and the right shifts of g for both Ir and Rh are found instead of the left shift with increasing T_e. Contrary to the case of Au, an electron delocalization from s block to d block with increasing T_e causes an increase of the electronic screening, which leads to a reduction of electron–ion potential. Therefore, the right shift of g is observed for Ir and Rh. The variations of g for Ir and Rh at high T_e are in accordance with the descriptions of iron (Fe) in Ref. [54], titanium (Ti) and tungsten (W) in Ref. [9]. However, as seen in the insets of Fig. 2(b)-(d), the evolution of μ with T_e toward higher energy is attributed to the preservation of constant number of valence electrons, as same as the case of Au. As a result, similar variations of f with the case of Au for Pd, Ir and Rh are shown in Fig. 2(b)-(d).

Although the difference of g with increasing T_e is seen for the case of

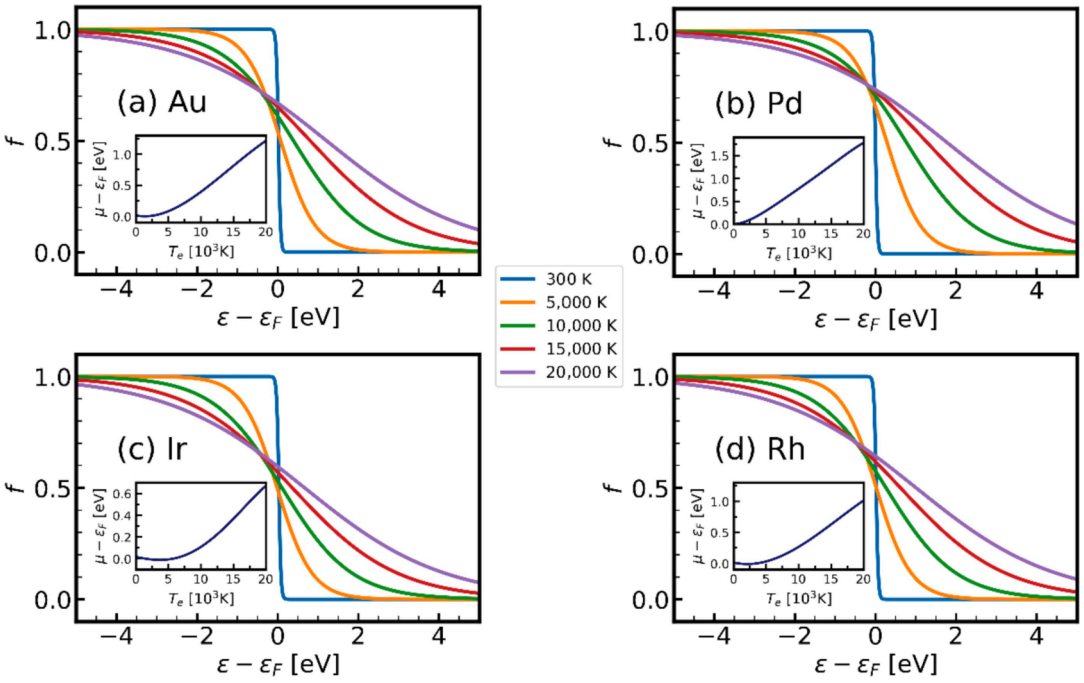

Fig. 2. Electron temperature T_e dependent f for (a) Au, (b) Pd, (c) Ir, and (d) Rh. Insets of (a)-(d) depict the changes of chemical potential μ to the Fermi energy ε_F, which affect the variations of f.

Ir and Rh, regarding those two metals as metals have free-electron-like electron structures is unreasonable. Only when the nearly parabolic band dependence of energy is observed, g of the noble metals get a good agreement with the free electron gas model. In addition, the invalidity of applying the free electron gas model is to be discussed in the next part.

3.2. Electron temperature dependent electron heat capacity

According to the calculation of C_e by Lin *et al.* [15], the impact of $\frac{\partial g|_{T_e}}{\partial T_e}$ was neglected in the expression of $C_e = \int_{-\infty}^{+\infty} \frac{\partial f(\varepsilon)}{\partial T_e} g(\varepsilon)\varepsilon d\varepsilon$, namely, constant g was applied in their calculation. Fig. 3(a)-(d) show the comparisons between $g|_{T_e}\varepsilon\frac{\partial f|_{T_e}}{\partial T_e}$ and $f|_{T_e}\varepsilon\frac{\partial g|_{T_e}}{\partial T_e}$ at several T_e for the given metals. The unneglectable effect of $f|_{T_e}\varepsilon\frac{\partial g|_{T_e}}{\partial T_e}$ in the expression of C_e is revealed within Eq. (1). Thus, the application of Eq. (2) considering both the effects of the T_e dependences of f and g, which effects are depicted in Eq. (1), is supposed to obtain a more precise result.

The calculation results of T_e dependent C_e from Eq. (2) are presented in Fig. 4(a)-(d). To verify the invalidity of the free electron gas model, the linear approximation derived by the free electron gas model is also plotted in Fig. 4(a)-(d) for each noble metal. Alternatively, the linear factor can also be determined by experiments [15,55].

Obviously, the linear T_e dependence of C_e is observed at T_e below 3, 000 K for Au, as shown in Fig. 4(a). The result shows excellent agreement with the linear approximation with $\gamma = \pi^2 k_B^2 g(\varepsilon_F)/3$ from the free electron gas model [15,16] and experiment with $\gamma = 67.6\ Jm^{-3}K^{-2}$ [56]. As discussed in the previous part, the accordance of the linear T_e dependence to the approximation and experiment is ascribed to the near-constant g and the little variation of f at low T_e in Eq. (1), in virtue of the little effect of excited 6s electrons. However, significant deviation from the linear approximation to the calculation result appears at high T_e. The deviation is attributed to the left shift of g due to the tremendous influence of substantial excited 5d electrons and the smearing of f with increasing T_e.

For comparison, the results of Holst *et al.* [8] and Lin *et al.* [15] are also plotted in Fig. 4(a) for Au. The result of Holst *et al.* [8] was obtained with similar expression to Eq. (2), the change of internal energy of the

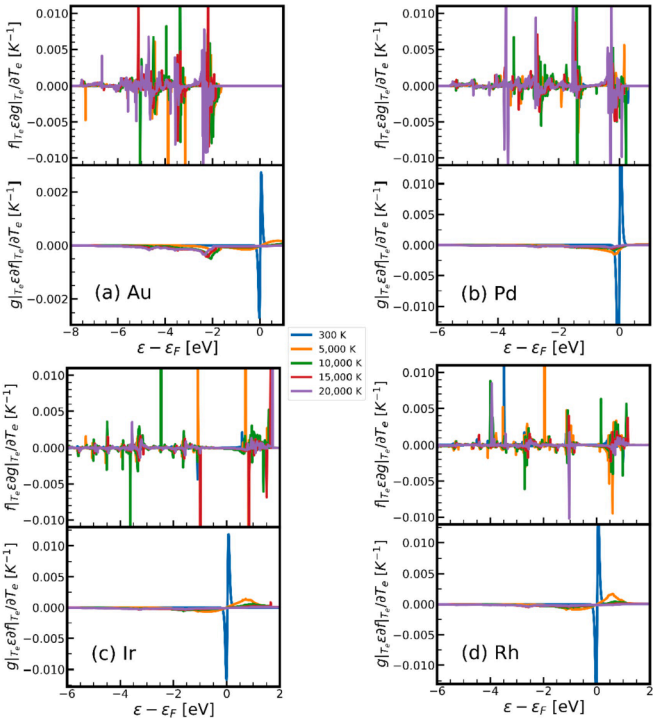

Fig. 3. Comparisons of $g|_{T_e}\varepsilon\frac{\partial f|_{T_e}}{\partial T_e}$ and $f|_{T_e}\varepsilon\frac{\partial g|_{T_e}}{\partial T_e}$ for (a) Au, (b) Pd, (c) Ir, and (d) Rh for electron temperature T_e at 300 K, 5, 000 K, 10, 000 K and 20, 000 K.

electron subsystem exhibits all aspects of the energy transportation procedure [8], containing the variation of g with T_e. In Fig. 4(a), C_e for Au almost coincides with that reported by Holst *et al.* [8]. The deviation from the present result to the result by Lin *et al.* [15] is based on the discussion of $g|_{T_e}\varepsilon\frac{\partial f|_{T_e}}{\partial T_e}$ and $f|_{T_e}\varepsilon\frac{\partial g|_{T_e}}{\partial T_e}$ above.

The effects of $f|_{T_e}\varepsilon\frac{\partial g|_{T_e}}{\partial T_e}$ for the other three metals are shown in Fig. 3

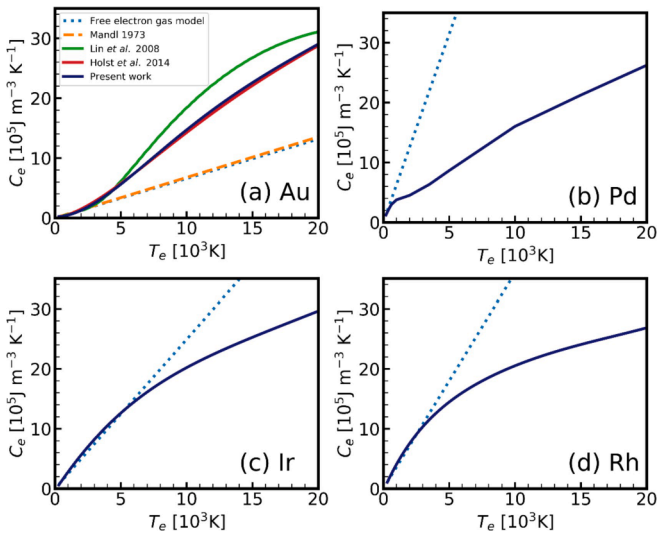

Fig. 4. Electron temperature T_e dependent electron heat capacity C_e for (a) Au, (b) Pd, (c) Ir, and (d) Rh. The curves are compared with several theoretical calculations and experimental results. For (a) Au: dotted line for linear factor $\gamma = \pi^2 k_B^2 g(\varepsilon_F)/3$ from the free electron gas model, dashed line for the linear factor $\gamma = 67.6\ Jm^{-3}K^{-2}$ from experiment [56], the calculation results by Holst *et al.* [8] and Lin *et al.* [15] are shown. For (b) Pd, (c) Ir and (d) Rh: dotted line for linear factor $\gamma = \pi^2 k_B^2 g(\varepsilon_F)/3$ from free-electron–gas model.

(b)-(d), thus the following calculations of T_e dependent C_e are deriving from the same framework for Au, shown in Fig. 4(b)-(d). In addition, the calculation from the free electron gas model is compared with the present model for these three metals. Similarly, by taking the same inference as Au, linear T_e dependence of C_e at low T_e is observed, getting a good agreement with the free electron gas model. At T_e below $1,000\ K$ for Pd, $5,000\ K$ for Ir and $3,000\ K$ for Rh, the calculated C_e show good agreements with the linear T_e dependent C_e by the free electron gas model. However, at high T_e, the effect of f should not be neglected for Pd, Ir, and Rh, as discussed previously. Contrary to the positive deviation from the linear T_e dependent C_e by the free electron gas model for Au, negative deviations of the calculated C_e for Pd, Ir and Rh are observed at high T_e. The behaviors are attributed to the different g for Au and other noble metals. Meanwhile, the smearing of f with increasing T_e is also a factor causing the deviations to the free electron gas model.

Therefore, in order to implement the nonlinear T_e dependent C_e for the noble metals, taking the impact of the components g and $f$into consideration is requisite [15,25]. In other words, the linear T_e dependent C_e by the free electron gas model is inappropriate to describe the femtosecond laser irradiation for the noble metals. Whereas, the approach to calculate T_e dependent C_e in the present study is a more precise path.

3.3. Electron temperature dependent electron-phonon coupling factor

Within Eq. (7), the evolution of G_{e-ph} is influenced by $g(\varepsilon_F)|_{T_e}$ and the integral $\int \left[g(\varepsilon)|_{T_e}\right]^2 \left(-\frac{\partial f|_{T_e}}{\partial \varepsilon}\right) d\varepsilon$ with the increasing T_e. Fig. 5(a)-(d) show the evolutions of the two components $\frac{1}{g(\varepsilon_F)|_{T_e}}$, and $\int \left[g(\varepsilon)|_{T_e}\right]^2 \left(-\frac{\partial f|_{T_e}}{\partial \varepsilon}\right) d\varepsilon$ with T_e. The tendency of the product of these two factors determined the tendency of T_e dependent G_{e-ph}, namely, $\frac{1}{g(\varepsilon_F)|_{T_e}}$ and $\int \left[g(\varepsilon)|_{T_e}\right]^2 \left(-\frac{\partial f|_{T_e}}{\partial \varepsilon}\right) d\varepsilon$ ought to be two crucial factors within the calculation of T_e dependent G_{e-ph}. Eventually, the calculation results of G_{e-ph} are presented in Fig. 6 (a)-(d).

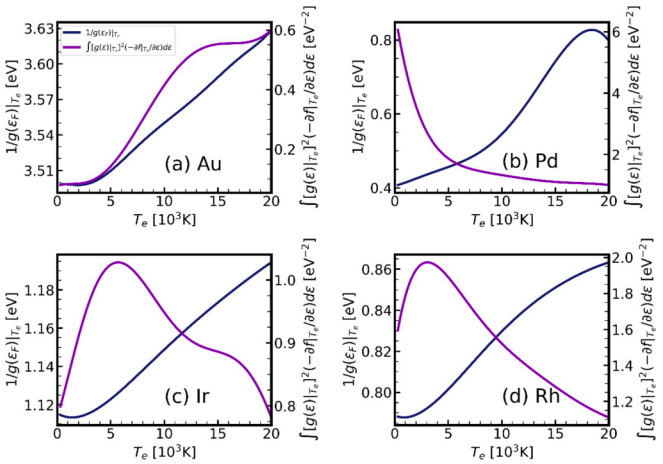

Fig. 5. The variations of the reciprocal of electron temperature T_e dependent electron density of states g at Fermi energy ε_F and the variations of the integral $\int \left[g(\varepsilon)|_{T_e}\right]^2 \left(-\frac{\partial f|_{T_e}}{\partial \varepsilon}\right) d\varepsilon$ with T_e in Eq. (7) for (a) Au, (b) Pd, (c) Ir, and (d) Rh.

The deviation of applying constant g and f is demonstrated explicitly in the previous part, thus accurate calculation of G_{e-ph} considering the impact of these two functions are shown directly. It is worth noting that f is regarded as step function at low T_e, thus Wang *et al.* [17] applied an approximation of T_e independent $G_{e-ph} = G_0 = \pi\hbar k_B g|_{T_e}(\varepsilon_F)\lambda\langle\omega^2\rangle$ to simplify the expression. In the present work, in order to avoid the relatively small absolute value of $-\partial f/\partial\varepsilon$ in Eq. (7) $\left(\langle 1\times 10^{-70}\right)$, the approximation from Wang *et al.* [17] is used merely for the case of $T_e < 1{,}000\ K$, for the purpose to ensure the accuracy of the calculation. Given the contribution of $-\frac{\partial f|_{T_e}}{\partial\varepsilon}\Big|_{\varepsilon=\varepsilon_F}$ in $\int \left[g(\varepsilon)|_{T_e}\right]^2 \left(-\frac{\partial f|_{T_e}}{\partial \varepsilon}\right) d\varepsilon$, it is narrow and gets a vast value at low T_e. By contrast, $-\frac{\partial f|_{T_e}}{\partial\varepsilon}\Big|_{\varepsilon=\varepsilon_F}$ extends and becomes smaller at high T_e. The feature of the component $-\partial f/\partial\varepsilon$ leads to the variation of $\int \left[g(\varepsilon)|_{T_e}\right]^2 \left(-\frac{\partial f|_{T_e}}{\partial \varepsilon}\right) d\varepsilon$, then affects G_{e-ph}.

For the case of Au, an ascending evolution of G_{e-ph} is observed with increasing T_e. For the reason that the high-energy edge of g for Au lo-

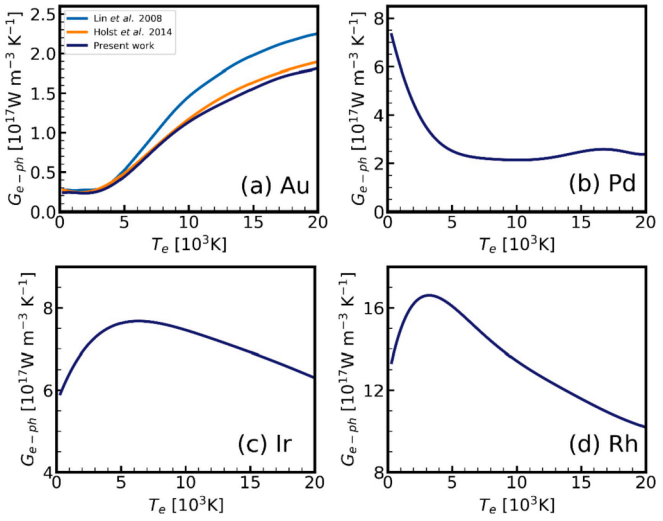

Fig. 6. Electron temperature T_e dependent electron–phonon coupling factor G_{e-ph} for (a) Au, (b) Pd, (c) Ir, and (d) Rh. For (a) Au, the curve is compared with several theoretical calculations, the calculation results by Holst *et al.* [8] and Lin *et al.* [15] are shown.

cates at the left of zero point and g keeps shifting to a lower energy with increasing T_e in Fig. 1(a), it is shown that both $1/g(\varepsilon_F)|_{T_e}$ and $\int\left[g(\varepsilon)|_{T_e}\right]^2\left(-\frac{\partial f|_{T_e}}{\partial\varepsilon}\right)d\varepsilon$ vary slightly at low T_e, thus the product of these components is near-constant, presented in Fig. 5(a). With the increase of T_e, growth tendency is observed within the evolutions of both $1/g(\varepsilon_F)|_{T_e}$ and $\int\left[g(\varepsilon)|_{T_e}\right]^2\left(-\frac{\partial f|_{T_e}}{\partial\varepsilon}\right)d\varepsilon$, hence their product shown a similar trend under the same circumstances. As a result, the variation of G_{e-ph} is accorded with the product of $\frac{1}{g(\varepsilon_F)|_{T_e}}$ and $\int\left[g(\varepsilon)|_{T_e}\right]^2\left(-\frac{\partial f|_{T_e}}{\partial\varepsilon}\right)d\varepsilon$, as shown in Fig. 6(a).

Noting that most of the experimental data from pump-probe experiment for Au were given by the correlation between experimental G_{e-ph} and laser fluence [29,30], thus the increment of T_e with absorbed laser energy is calculated by the $T_e-\Delta E$ function from [8]. At T_e below 2,500 K, a near-constant value for Au $G_{e-ph}|_{T_e<2{,}500\ K}\approx 2.39\times10^{16}\ W/K^{-1}m^{-3}$ agrees well with the experimental values $(2.1\pm0.2)\times10^{16}\ W/K^{-1}m^{-3}$ [29] and $2.2\times10^{16}\ W/K^{-1}m^{-3}$ [30]. At higher T_e, a huge gap between the calculated result $G_{e-ph}|_{T_e\approx15{,}000\ K}=15.59\times10^{16}\ W/K^{-1}m^{-3}$ and the experimental value $(4.9\pm1)\times10^{16}\ W/K^{-1}m^{-3}$ [30] is observed. However, the calculated result of G_{e-ph} for Au get a good agreement with the result from Holst *et al.* [8]. Nevertheless, a slight positive deviation of the calculated G_{e-ph} is observed with the results of Lin *et al.* [15]. The deviation is attributed to the difference of $\lambda\langle\omega^2\rangle$ and the contribution of T_e dependent g.

On account of there is rare research on G_{e-ph} for Pd, Ir and Rh, the deviations of $\lambda\langle\omega^2\rangle$ with increasing T_e for these noble metals were neglected, as similar as the case of Au. The evolutions of two crucial components $1/g(\varepsilon_F)|_{T_e}$ and $\int\left[g(\varepsilon)|_{T_e}\right]^2\left(-\frac{\partial f|_{T_e}}{\partial\varepsilon}\right)d\varepsilon$ to T_e dependent G_{e-ph} for these noble metals are plotted in Fig. 5(b)-(d). Obviously, the slow growth tendency of $\frac{1}{g(\varepsilon_F)|_{T_e}}$ with increasing T_e is observed, as similar as the case of Au. But the evolutions of $\int\left[g(\varepsilon)|_{T_e}\right]^2\left(-\frac{\partial f|_{T_e}}{\partial\varepsilon}\right)d\varepsilon$ are distinct between them. For Pd, a dramatic decrease of $\int\left[g(\varepsilon)|_{T_e}\right]^2\left(-\frac{\partial f|_{T_e}}{\partial\varepsilon}\right)d\varepsilon$ is observed at low T_e, and it turns steady at high T_e. In addition, a slight fallback of $\frac{1}{g(\varepsilon_F)|_{T_e}}$ is observed at $T_e\approx 7{,}500\ K$. Thus, the variation of T_e dependent G_{e-ph} decreases at low T_e and turns steady until $T_e\approx 7{,}500\ K$, the slight fall back of $\frac{1}{g(\varepsilon_F)|_{T_e}}$ causes same behavior of G_{e-ph}, as shown in Fig. 6(b).

For both Ir and Rh, peaks of $\int\left[g(\varepsilon)|_{T_e}\right]^2\left(-\frac{\partial f|_{T_e}}{\partial\varepsilon}\right)d\varepsilon$ are observed at $T_e\approx 7{,}500\ K$ and $T_e\approx 2{,}500\ K$ respectively. Owing to more significant changes of $\int\left[g(\varepsilon)|_{T_e}\right]^2\left(-\frac{\partial f|_{T_e}}{\partial\varepsilon}\right)d\varepsilon$ than $\frac{1}{g(\varepsilon_F)|_{T_e}}$ with increasing T_e, the evolutions of T_e dependent G_{e-ph} demonstrate similar behavior with the evolutions of $\int\left[g(\varepsilon)|_{T_e}\right]^2\left(-\frac{\partial f|_{T_e}}{\partial\varepsilon}\right)d\varepsilon$, as shown in Fig. 6(c)-(d).

In addition, the calculation results of G_{e-ph} for Pd, Ir, and Rh shown a great agreement with Ref. [52] at low T_e. The calculation results at room temperature $7.29\times10^{17}\ W/K^{-1}m^{-3}$ for Pd, $6.03\times10^{17}\ W/K^{-1}m^{-3}$ for Ir and $13.48\times10^{17}\ W/K^{-1}m^{-3}$ for Rh, are comparable to $7.4\times10^{17}\ W/K^{-1}m^{-3}$ for Pd, $6.0\times10^{17}\ W/K^{-1}m^{-3}$ for Ir and $13.3\times10^{17}\ W/K^{-1}m^{-3}$ for Rh [52].

High magnitude of G_{e-ph} indicates strong electron–phonon interaction, the value of $\lambda\langle\omega^2\rangle$ demonstrates the extent of the interaction strength. For Au, $\lambda\langle\omega^2\rangle=21.5\ meV^2$ is obtained and used in the calculating G_{e-ph}. The result from the present model agrees well with the calculation result $\lambda\langle\omega^2\rangle=21\pm2\ meV^2$ by Holst *et al.* [8] and the experimental value $\lambda\langle\omega^2\rangle=23\pm4\ meV^2$ reported by Lin *et al.* [15]. Likewise, the values of $\lambda\langle\omega^2\rangle$ for Pd, Ir, and Rh are obtained. The results are 66.38 meV^2 for Pd, 144.36 meV^2 for Ir, and 221.18 meV^2 for Rh. Obviously, the strength of electron–phonon interaction for Au is weaker than the other three metals due to smaller value of $\lambda\langle\omega^2\rangle$. But growth trend of G_{e-ph} of Au is observed with the increasing T_e. However, regress trend of G_{e-ph} for Pd, Ir, and Rh with the increasing T_e are found, as shown in Fig. 5(b)-(d).

4. Conclusion

To sum up, theoretical calculations and analyses of C_e and G_{e-ph} for Au, Pd, Ir, and Rh with an *ab initio* method are presented. Based on the discussions of electron excitation induced by femtosecond laser irradiation, the variations of g are observed. The further calculation of C_e and G_{e-ph} are affected by the variation g and f. Given the comparison between the calculated C_e and the C_e by the free electron gas model, there are tremendous deviations from the present *ab initio* calculation to the free electron gas model due to the T_e dependent g. Namely, the free electron gas model is inappropriate for the noble metals. For the case of Au, the calculated C_e and G_{e-ph} are affected by the excited d electrons when T_e exceed 3,000 K. Moreover, the calculation results for Au are in accordance with those from experiment and simulation, which proves the feasibility and utility of employing the same approach to calculate C_e and G_{e-ph} of Pd, Ir, and Rh. Due to the difference between the location of the high-energy edge of g of Pd and Au, the calculated C_e increases and the caculated G_{e-ph} decreases with increasing T_e. For the cases of Ir and Rh, though the calculated C_e shown increasing tendency with the increase of T_e, it presents more complex evolutions of the calculated G_{e-ph} for these two metals than that for Au. It can be explained by the huge distinctions of g between Ir and Rh to Au. Calculation results in the present study is informative to the production of nanoparticles by femtosecond laser ablation for noble metals. Among the process, C_e and G_{e-ph} are the two key parameters to describe the femtosecond laser-induced electron excitation and the electron–phonon coupled thermal energy transportation.

CRediT authorship contribution statement

Yongnan Li: Investigation, Formal analysis, Project administration, Writing – original draft. **Pengfei Ji:** Supervision, Project administration, Conceptualization, Methodology, Writing – review & editing.

Declaration of Competing Interest

The authors declare that they have no known competing financial interests or personal relationships that could have appeared to influence the work reported in this paper.

Acknowledgments

Support for this work by the National College Students Innovation and Entrepreneurship Training Program under grant number BIT262201116 and the National Natural Science Foundation of China under grant number 51705234 are gratefully acknowledged.

Appendix A. Supplementary data

Supplementary data to this article can be found online at https://doi.org/10.1016/j.commatsci.2021.110959.

References

[1] P. Balling, J. Schou, Femtosecond-laser ablation dynamics of dielectrics: basics and applications for thin films, Reports Prog. Phys. 76 (3) (2013) 036502, https://doi.org/10.1088/0034-4885/76/3/036502.

[2] Y. Dubi, Y. Sivan, "Hot" electrons in metallic nanostructures—non-thermal carriers or heating? Light Sci. Appl. 8 (1) (2019) https://doi.org/10.1038/s41377-019-0199-x.

[3] S. Yabuuchi, Y. Kurosaki, N. Fukatani, J. Hayakawa, First-principles study of electron-phonon coupling factor and lattice thermal conductivity of L12 type alloys, Mater. Today Proc. 44 (2021) 3445–3449, https://doi.org/10.1016/j.matpr.2020.02.386.

[4] S. Li, Z. Tong, X. Zhang, H. Bao, Thermal conductivity and Lorenz ratio of metals at intermediate temperatures with mode-level first-principles analysis, Phys. Rev. B. 102 (2020), 174306, https://doi.org/10.1103/PhysRevB.102.174306.

[5] J.G. Horstmann, H. Böckmann, B. Wit, F. Kurtz, G. Storeck, C. Ropers, Coherenat control of a surface structural phase transition, Nature 583 (2020) 232–236, https://doi.org/10.1038/s41586-020-2440-4.

[6] N. Medvedev, I. Milov, Electron-phonon coupling in metals at high electronic temperatures, Phys. Rev. B. 102 (2020) 1–22, https://doi.org/10.1103/PhysRevB.102.064302.

[7] N.A. Smirnov, Copper, gold, and platinum under femtosecond irradiation: results of first-principles calculations, Phys. Rev. B. 101 (9) (2020), https://doi.org/10.1103/PhysRevB.101.094103.

[8] B. Holst, V. Recoules, S. Mazevet, M. Torrent, A. Ng, Z. Chen, S.E. Kirkwood, V. Sametoglu, M. Reid, Y.Y. Tsui, Ab initio model of optical properties of two-temperature warm dense matter, Phys. Rev. B. 90 (2014) 1–9, https://doi.org/10.1103/PhysRevB.90.035121.

[9] E. Bévillon, J.P. Colombier, V. Recoules, R. Stoian, Free-electron properties of metals under ultrafast laser-induced electron-phonon nonequilibrium: a first-principles study, Phys. Rev. B. 89 (2014) 1–11, https://doi.org/10.1103/PhysRevB.89.115117.

[10] P. Ji, Y. Zhang, Ab initio determination of effective electron – phonon coupling factor in copper, Phys. Lett. A. 380 (17) (2016) 1551–1555, https://doi.org/10.1016/j.physleta.2016.02.044.

[11] Y. Rong, P. Ji, M. He, Y. Zhang, Y. Tang, Multiscale investigation of femtosecond laser pulses processing aluminum in burst mode, Nanoscale Microscale Thermophys. Eng. 22 (4) (2018) 324–347, https://doi.org/10.1080/15567265.2018.1497111.

[12] B. Rethfeld, D.S. Ivanov, M.E. Garcia, S.I. Anisimov, Modelling ultrafast laser ablation, J. Phys. D. Appl. Phys. 50 (19) (2017) 193001, https://doi.org/10.1088/1361-6463/50/19/193001.

[13] S.I. Anisimov, B.L. Kapeliovich, T.L. Perelman, Electron emission from metal surfaces exposed to ultrashort laser pulses, Zhurnal Eksp. i Teor Fiz. 66 (1974) 776–781.

[14] P. Ji, Y. Zhang, Continuum-atomistic simulation of picosecond laser heating of copper with electron heat capacity from ab initio calculation, Chem. Phys. Lett. 648 (2016) 109–113, https://doi.org/10.1016/j.cplett.2016.02.003.

[15] Z. Lin, L.V. Zhigilei, V. Celli, Electron-phonon coupling and electron heat capacity of metals under conditions of strong electron-phonon nonequilibrium, Phys. Rev. B. 77 (7) (2008), https://doi.org/10.1103/PhysRevB.77.075133.

[16] N.W. Ashcroft, M.N. David, Solid State Physics, Cengage Learning, 1976.

[17] X.Y. Wang, D.M. Riffe, Y.-S. Lee, M.C. Downer, Time-resolved electron-temperature measurement in a highly excited gold target using femtosecond thermionic emission, Phys. Rev. B. 50 (1994) 8016–8019, https://doi.org/10.1017/CBO9781107415324.004.

[18] Allen, Theory of thermal relaxation of electrons in metals, Phys. Rev. Lett. 59 (1987) 5237, https://doi.org/10.1103/PhysRevLett.84.5237.

[19] Y. Son, J. Yeo, H. Moon, T.W. Lim, S. Hong, K.H. Nam, S. Yoo, C.P. Grigoropoulos, D.-Y. Yang, S.H. Ko, Nanoscale electronics: digital fabrication by direct femtosecond laser processing of metal nanoparticles, Adv. Mater. 23 (28) (2011) 3176–3181, https://doi.org/10.1002/adma.v23.2810.1002/adma.201100717.

[20] S. Mazevet, M. Torrent, V. Recoules, F. Jollet, Calculations of the transport properties within the PAW formalism, High Energy Density Phys. 6 (1) (2010) 84–88, https://doi.org/10.1016/j.hedp.2009.06.004.

[21] C. Gadermaier, A.S. Alexandrov, V.V. Kabanov, P. Kusar, T. Mertelj, X. Yao, C. Manzoni, D. Brida, G. Cerullo, D. Mihailovic, Electron-phonon coupling in high-temperature cuprate superconductors determined from electron relaxation rates, Phys. Rev. Lett. 105 (2010) 1–4, https://doi.org/10.1103/PhysRevLett.105.257001.

[22] X. Gonze, B. Amadon, P.-M. Anglade, J.-M. Beuken, F. Bottin, P. Boulanger, F. Bruneval, D. Caliste, R. Caracas, M. Côté, T. Deutsch, L. Genovese, P. Ghosez, M. Giantomassi, S. Goedecker, D.R. Hamann, P. Hermet, F. Jollet, G. Jomard, S. Leroux, M. Mancini, S. Mazevet, M.J.T. Oliveira, G. Onida, Y. Pouillon, T. Rangel, G.-M. Rignanese, D. Sangalli, R. Shaltaf, M. Torrent, M.J. Verstraete, G. Zerah, J.W. Zwanziger, ABINIT: First-principles approach to material and nanosystem properties, Comput. Phys. Commun. 180 (12) (2009) 2582–2615, https://doi.org/10.1016/j.cpc.2009.07.007.

[23] P.E. Hopkins, P.M. Norris, R.J. Stevens, T.E. Beechem, S. Graham, Influence of interfacial mixing on thermal boundary conductance across a chromium/silicon interface, J. Heat Transfer. 130 (2008), https://doi.org/10.1115/1.2891159.

[24] N. Shokoufi, F. Shemirani, Laser induced-thermal lens spectrometry after cloud point extraction for the determination of trace amounts of rhodium, Talanta 73 (4) (2007) 662–667, https://doi.org/10.1016/j.talanta.2007.04.035.

[25] V. Recoules, J. Clérouin, G. Zérah, P.M. Anglade, S. Mazevet, Effect of intense laser irradiation on the lattice stability of semiconductors and metals, Phys. Rev. Lett. 96 (2006) 1–4, https://doi.org/10.1103/PhysRevLett.96.055503.

[26] J.K. Chen, W.P. Latham, J.E. Beraun, The role of electron–phonon coupling in ultrafast laser heating, J. Laser Appl. 17 (1) (2005) 63–68, https://doi.org/10.2351/1.1848522.

[27] A. Jain, A.J.H. McGaughey, Thermal transport by phonons and electrons in aluminum, silver, and gold from first principles, Phys. Rev. B. 93 (2016), 081206, https://doi.org/10.1103/PhysRevB.93.081206.

[28] A.M. Brown, R. Sundararaman, P. Narang, W.A. Goddard, H.A. Atwater, Ab initio phonon coupling and optical response of hot electrons in plasmonic metals, Phys. Rev. B. 94 (2016), 075120, https://doi.org/10.1103/PhysRevB.94.075120.

[29] J. Hohlfeld, S.-S. Wellershoff, J. Güdde, U. Conrad, V. Jähnke, E. Matthias, Electron and lattice dynamics following optical excitation of metals, Chem. Phys. 251 (1-3) (2000) 237–258, https://doi.org/10.1016/S0301-0104(99)00330-4.

[30] M.Z. Mo, Z. Chen, R.K. Li, M. Dunning, B.B.L. Witte, J.K. Baldwin, L.B. Fletcher, J. B. Kim, A. Ng, R. Redmer, A.H. Reid, P. Shekhar, X.Z. Shen, M. Shen, K. Sokolowski-Tinten, Y.Y. Tsui, Y.Q. Wang, Q. Zheng, X.J. Wang, S.H. Glenzer, Heterogeneous to homogeneous melting transition visualized with ultrafast electron diffraction, Science (6369) (2018) 3601451–3601455, https://doi.org/10.1126/science.aar2058.

[31] J.J. Paggel, T. Miller, T.-C. Chiang, Temperature dependent complex band structure and electron-phonon coupling in Ag, Phys. Rev. Lett. 83 (7) (1999) 1415–1418, https://doi.org/10.1103/PhysRevLett.83.1415.

[32] W. Miao, M. Wang, Nonequilibrium effects on the electron-phonon coupling constant in metals, Phys. Rev. B. 103 (2021), 125412, https://doi.org/10.1103/PhysRevB.103.125412.

[33] H. Jang, J. Kimling, D.G. Cahill, Nonequilibrium heat transport in Pt and Ru probed by an ultrathin Co thermometer, Phys. Rev. B. 101 (2020), 064304, https://doi.org/10.1103/PhysRevB.101.064304.

[34] E. Eser, H. Koç, Investigations of temperature dependences of electrical resistivity and specific heat capacity of metals, Phys. B Condens. Matter. 492 (2016) 7–10, https://doi.org/10.1016/J.PHYSB.2016.03.032.

[35] S. Babar, J.H. Weaver, Optical constants of Cu, Ag, and Au revisited, Appl. Opt. 54 (2015) 477–481, https://doi.org/10.1364/AO.54.000477.

[36] J.C. Idrobo, S.T. Pantelides, Origin of bulklike optical response in noble-metal Ag and Au nanoparticles, Phys. Rev. B. 82 (2010) 85420, https://doi.org/10.1103/PhysRevB.82.085420.

[37] L. Uba, S. Uba, V.N. Antonov, Magneto-optical Kerr spectroscopy of noble metals, Phys. Rev. B. 96 (2017), 235132, https://doi.org/10.1103/PhysRevB.96.235132.

[38] R. Sato, M. Ohnuma, K. Oyoshi, Y. Takeda, Experimental investigation of nonlinear optical properties of Ag nanoparticles: effects of size quantization, Phys. Rev. B. 90 (2014), 125417, https://doi.org/10.1103/PhysRevB.90.125417.

[39] A. Kumar, A. Kumar, P.K. Ahluwalia, Electronic and optical properties of free standing Pt nanowires using localized basis sets, AIP Conf. Proc. 1447 (2012) 831–832, https://doi.org/10.1063/1.4710260.

[40] J.R. Kitchin, J.K. Nørskov, M.A. Barteau, J.G. Chen, Modification of the surface electronic and chemical properties of Pt(111) by subsurface 3d transition metals, J. Chem. Phys. 120 (21) (2004) 10240–10246, https://doi.org/10.1063/1.1737365.

[41] E. Gharibshahi, E. Saion, A. Ashraf, L. Gharibshahi, Size-controlled and optical properties of platinum nanoparticles by gamma radiolytic synthesis, Appl. Radiat. Isot. 130 (2017) 211–217, https://doi.org/10.1016/j.apradiso.2017.09.012.

[42] V. Balaram, Environmental Impact of Platinum, Palladium, and Rhodium Emissions from Autocatalytic Converters – A Brief Review of the Latest Developments, in: Handb. Environ. Mater. Manag, Springer, Cham, 2020, pp. 1–37, https://doi.org/10.1007/978-3-319-58538-3_194-1.

[43] T. Nishi, A. Takeichi, H. Azuma, N. Suzuki, T. Hioki, T. Motohiro, Fabrication of palladium nanoparticles by laser ablation in liquid, J. Laser Micro Nanoeng. 5 (2010) 192–196, https://doi.org/10.2961/jlmn.2010.03.0002.

[44] L. Zhang, Q. Chang, H. Chen, M. Shao, Recent advances in palladium-based electrocatalysts for fuel cell reactions and hydrogen evolution reaction, Nano Energy 29 (2016) 198–219, https://doi.org/10.1016/j.nanoen.2016.02.044.

[45] Z. Chen, X. Duan, W. Wei, S. Wang, B.-J. Ni, Iridium-based nanomaterials for electrochemical water splitting, Nano Energy 78 (2020) 105270, https://doi.org/10.1016/j.nanoen.2020.105270.

[46] P. Jovanovič, N. Hodnik, F. Ruiz-Zepeda, I. Arčon, B. Jozinović, M. Zorko, M. Bele, M. Šala, V.S. Šelih, S. Hočevar, M. Gaberšček, Electrochemical dissolution of iridium and iridium oxide particles in acidic media: transmission electron microscopy, electrochemical flow cell coupled to inductively coupled plasma mass spectrometry, and X-ray absorption spectroscopy study, J. Am. Chem. Soc. 139 (36) (2017) 12837–12846, https://doi.org/10.1021/jacs.7b08071.

[47] V. Balaram, Environmental Impact of Platinum, Palladium, and Rhodium Emissions from Autocatalytic Converters – A Brief Review of the Latest Developments, in: C.M. Hussain (Ed.), Handb. Environ. Mater. Manag, Springer International Publishing, Cham, 2020, pp. 1–37, https://doi.org/10.1007/978-3-319-58538-3_194-1.

[48] U. Zywietz, C. Reinhardt, A.B. Evlyukhin, T. Birr, B.N. Chichkov, Generation and patterning of Si nanoparticles by femtosecond laser pulses, Appl. Phys. A Mater. Sci. Process. 114 (1) (2014) 45–50, https://doi.org/10.1007/s00339-013-8007-6.

[49] M.S. Satya Bharati, B. Chandu, S.V. Rao, Explosives sensing using Ag-Cu alloy nanoparticles synthesized by femtosecond laser ablation and irradiation, RSC Adv. 9 (3) (2019) 1517–1525, https://doi.org/10.1039/C8RA08462A.

[50] T. Tsuji, T. Kakita, M. Tsuji, Preparation of nano-size particles of silver with femtosecond laser ablation in water, Appl. Surf. Sci. 206 (1-4) (2003) 314–320, https://doi.org/10.1016/S0169-4332(02)01230-8.

[51] J. Guan, X. Wen, Q. Zhang, Z. Duan, Atomic rhodium catalysts for hydrogen evolution and oxygen reduction reactions, Carbon N. Y. 164 (2020) 121–128, https://doi.org/10.1016/j.carbon.2020.03.055.
[52] D.A. Papaconstantopoulos, Handbook of the Band Structure of Elemental Solids, Springer, US, Boston, 2015, 10.1007/978-1-4419-8264-3_1.
[53] X. Gonze, J.-M. Beuken, R. Caracas, F. Detraux, M. Fuchs, G.-M. Rignanese, L. Sindic, M. Verstraete, G. Zerah, F. Jollet, M. Torrent, A. Roy, M. Mikami, P. Ghosez, J.-Y. Raty, D.C. Allan, First-principles computation of material properties: The ABINIT software project, Comput. Mater. Sci. 25 (3) (2002) 478–492, https://doi.org/10.1016/S0927-0256(02)00325-7.
[54] E. Bévillon, J.P. Colombier, B. Dutta, R. Stoian, Ab initio nonequilibrium thermodynamic and transport properties of ultrafast laser irradiated 316l stainless steel, J. Phys. Chem. C. 119 (21) (2015) 11438–11446, https://doi.org/10.1021/acs.jpcc.5b02085.
[55] S. Lei, X. Zhao, X. Yu, A. Hu, S. Vukelic, M.B.G. Jun, H.-E. Joe, Y.L. Yao, Y.C. Shin, Ultrafast Laser Applications in Manufacturing Processes: A State of the Art Review, ASME 2019 14th Int. Manuf. Sci. Eng. Conf. MSEC 2019. 2 (2019). https://doi.org/10.1115/MSEC2019-2968.
[56] F. Mandl, American Institute of Physics Handbook, Phys. Bull. 24 (1973) 492, https://doi.org/10.1088/0031-9112/24/8/017.